Article

Photoconduction Properties in Tungsten Disulfide Nanostructures

Hemanth Kumar Bangolla [1] [ID], **Yueh-Chien Lee** [2], **Wei-Chu Shen** [3], **Rajesh Kumar Ulaganathan** [4] [ID], **Raman Sankar** [4], **He-Yun Du** [5],* **and Ruei-San Chen** [1],*

[1] Graduate Institute of Applied Science and Technology, National Taiwan University of Science and Technology, Taipei 10607, Taiwan; hemanthbangolla@gmail.com

[2] Department of Electronic Engineering, Lunghwa University of Science and Technology, Taoyuan 33306, Taiwan; yclee8858@gmail.com

[3] Department of Electronic Engineering, National Taiwan University of Science and Technology, Taipei 10607, Taiwan; m10202337@mail.ntust.edu.tw

[4] Institute of Physics, Academia Sinica, Taipei 115201, Taiwan; urajeshkumariitr@gmail.com (R.K.U.); sankarndf@gmail.com (R.S.)

[5] Department of Chemical Engineering, Ming Chi University of Technology, New Taipei City 24301, Taiwan

* Correspondence: heyundu@mail.mcut.edu.tw (H.-Y.D.); rsc@mail.ntust.edu.tw (R.-S.C.)

Abstract: We reported the photoconduction properties of tungsten disulfide (WS_2) nanoflakes obtained by the mechanical exfoliation method. The photocurrent measurements were carried out using a 532 nm laser source with different illumination powers. The results reveal a linear dependence of photocurrent on the excitation power, and the photoresponsivity shows an independent behavior at higher light intensities (400–4000 Wm^{-2}). The WS_2 photodetector exhibits superior performance with responsivity in the range of 36–73 AW^{-1} and a normalized gain in the range of 3.5–7.3 10^{-6} cm^2V^{-1} at a lower bias voltage of 1 V. The admirable photoresponse at different light intensities suggests that WS_2 nanostructures are of potential as a building block for novel optoelectronic device applications.

Keywords: tungsten disulfide; nanoflake; photoconductivity; photodetector; responsivity; normalized gain

1. Introduction

In the modern technology era, optoelectronic devices have been established as one of the most ambitious fields of study. Photodetectors are the sub-class of optoelectronic devices that can convert incident light into electrical signals precisely. Photodetectors are vital components to achieve devices with multi-functionality, and hence gained more attention in many applications such as imaging, optical communications, light sensing, and biomedical instruments [1–3]. Photodetectors can be divided into two categories based on detection mechanism, namely, photon or quantum detectors and thermal detectors. The photon detectors that include photoconductors, photodiodes, and photo-field effect transistors (photo-FETs) are widely studied due to the existence of band gaps and fast inter-band optical transition. The thermal detectors are either bolometers or thermopiles. Due to their indirect photoelectric conversion, thermal detectors have a relatively slow photoresponse speed [4]. A photoconductor is a fundamental photodetector that is simply a semiconductor channel with ohmic contacts on both ends that works on a photoconductive effect. The photoconductive effect is a process in which the conductivity of a semiconductor material increases due to photon absorption when illuminated by light energy larger than the bandgap of the semiconductor. A photoconductor possesses a gain that can be greater than unity. The high gain will reduce the response speed of the photoconductor. In order to achieve a photoconductor's desired overall performance, a trade-off between gain and response speed must be made [5].

The advent of nanomaterials leads to improving the performance and shrinking the size of novel devices due to their exceptional properties governed by high surface-to-

volume ratio and quantum effects at a nanoscale regime [3]. Recently, the transition metal dichalcogenides (TMDs) belonging to the two-dimensional (2D) family have been promoted as novel candidates for fabricating miniature electronic and optoelectronic devices for next-generation devices due to their excellent electrical and optical properties [6–11]. The 2D TMDs have a honeycomb molecular structure of MX_2, where M is a transition metal atom and X is a chalcogen atom. In 2D TMDs, the strong covalent bonded layers are stacked via weak van der Wall interactions. Among the TMDs, the most extensive research has been done on molybdenum disulfide (MoS_2). The first mono-layered MoS_2 phototransistor exhibits a fast response time of 50 ms, but shows a low responsivity of 7 mAW^{-1} due to its poor carrier mobility and low optical absorbance [12]. The multi-layered MoS_2 photodetectors show a responsivity in the range of 100–570 mAW^{-1} due to the increase of optical absorbance of multilayers [13,14].

The versatile compound tungsten disulfide (WS_2), another promising member of the TMDs group, has been widely investigated in the field of optoelectronic device applications due to its high mobility and environmental stability [15–19]. The WS_2 possesses an indirect bandgap (1.4 eV) in its bulk form, and it converts to a direct bandgap (2.1 eV) for a monolayer [20,21]. Moreover, WS_2 has strong optical absorption, high spin-orbit coupling, and high photoluminescence and can be operated over wide temperatures [22–24]. The theoretical calculations suggest WS_2 has a smaller electron-effective mass and thus has higher carrier mobility [25,26]. Each layer in the WS_2 compound is composed of tungsten (W) atoms sandwiched between the sulfur (S) atoms (S-W-S). Hence, the WS_2 bulk crystal consists of stacks of three atom sheets. It can be easily exfoliated into thin nanoflakes or nanosheets with strong in-plane covalent bonding and transferred onto an arbitrary substrate due to the weak van der Waals force between various sheets [27,28]. The exfoliated WS_2 monolayers or multilayers attained exceptional significance in various applications such as photodetectors [22], field effect transistors [29], gas sensors [30], energy storage devices [31], light emitting diode elements [32], and catalysts [33]. The light absorption in monolayer TMDs is approximately 5–10% in the visible regime [34]. This is relatively higher than the conventional photodetector materials such as Si and GaAs in a comparable thickness [35]. However, the practical applications of monolayer TMDs have been restricted due to their thickness-limited absorption, bandgap-limited spectral response, and high Schottky barrier-limited charge collection efficiency [36]. In the WS_2 monolayer, the conduction band (CB) edge is located at a higher energy than that of a MoS_2 monolayer. This results in more severe issues in electrical contact as it forms higher Schottky barriers between WS_2 and metal electrodes as compared to MoS_2 [15]. Unlike monolayer TMDs, the thicker multilayer TMDs possess better electrical transport and higher light absorption coefficients [37,38]. Hence, the photodetectors based on multilayer TMDs can be achieved with high responsivity and a wide spectral regime [13,26].

The 2D WS_2 material can be synthesized by both top-down and bottom-up approaches. The widely used top-down techniques are mechanical exfoliation, chemical/liquid exfoliation, and laser or electron irradiation. The bottom-up techniques that include chemical vapor deposition (CVD), atomic layer deposition (ALD), hydrothermal or electrochemical process, and molecular beam epitaxy (MBE) have been extensively studied [39]. In general, the synthesis technique should be simple, affordable, and scalable without the need for expensive machinery for low-cost production. Among the above-mentioned techniques, the mechanical exfoliation method is simple and does not require any sophisticated instruments. The exfoliation also produces nanoflakes with high crystalline quality [38]. In the exfoliation technique, the nanoflakes were peeled from the bulk crystals using scotch tape. A few reports are available on the photoresponse behavior of mechanically exfoliated 2D WS_2 [3]. Lee et al. reported FET based on multi-layer WS_2 with a thickness of ~20 nm and a photoresponsivity of ~0.27 A/W [40]. Huo et al. reported multilayered WS_2 nanoflakes-based FET with a photoresponsivity of 5.7 A/W [30]. Huo et al. also reported a transistor based on a multi-layer MoS_2–WS_2 heterostructure. The planar device exhibits a photoresponsivity of 1.42 A/W [41].

In this work, the WS$_2$ nanoflakes are exfoliated from the chemical vapor transport (CVT) grown crystals using a conventional mechanical exfoliation technique. For the fabrication of a photoconductor-type photodetector, the platinum (Pt) electrodes were deposited on a WS$_2$ nanoflake using the focused ion beam (FIB) technique. The photoconduction properties of the device were investigated under the laser wavelength of 532 nm with different powers. The fabricated device shows good performance at a lower bias voltage of 1 V. The photodetector parameters such as responsivity, gain, and normalized gain were estimated and discussed.

2. Materials and Methods

2.1. WS$_2$ Crystal Growth

Single crystals of WS$_2$ were grown by the CVT method using the fine powders of sulfur (99.99%) and tungsten (99.99%) with the help of iodine (I$_2$) as a transporting agent. At first, sulfur and tungsten powders were mixed with I$_2$ and transferred into the quartz ampoule with a length of 30 cm. The inner and outer diameter of the quartz ampoule is 1.3 and 1.6 cm, respectively. Later, the quartz ampoule was evacuated to 10^{-5} Torr and sealed at one end. Next, the sealed ampoule was kept in the two-zone horizontal furnace maintained at temperatures of 1020 and 960 °C. The precursor powder was kept at the higher temperature of 1020 °C zone; once the powder started to melt and vaporize, the I$_2$ transported the vaporized precursor to the other end of the tube; the temperature was maintained at 960 °C. After ten days of the process, the vaporized precursors were deposited as single crystals of 1–2 cm in length.

2.2. Fabrication of WS$_2$ Photodetector

The WS$_2$ nanoflakes were exfoliated from the bulk crystal using a conventional mechanical exfoliation technique using dicing tape. For the fabrication of a photoconductor-type photodetector, the WS$_2$ nanoflakes were transferred onto a SiO$_2$ (300 nm)/n$^+$-Si substrate with pre-patterned Ti/Au electrodes. Next, two Pt metal contacts with a thickness of 100 nm were deposited on WS$_2$ nanoflakes using the FIB technique. Finally, the electrical wires were connected to the Ti/Au electrodes using a silver paste to characterize the fabricated device. The Ti/Au electrodes are the interconnection between the Pt microelectrode and the millimeter-sized bonded wire.

### 2.3. Measurements and Characterization

The X-ray diffraction (XRD) pattern was measured using a D2 Phaser X-ray diffractometer, and the Raman spectroscopy was measured with an excitation wavelength of 532 nm using a Raman microscope (Renishaw InVia, Wotton-under-Edge, UK); these measurements were used to confirm the crystal structure of CVT-grown WS$_2$ crystals. The height profiles were carried out to find the thickness of nanoflakes using atomic force microscopy (AFM, Bruker-ICON2-SYS, Billerica, MA, USA). Scanning electron microscopy (SEM, Hitachi S3000H, Tokyo, Japan) was used to capture the image of the nanoflake device to obtain the dimensions of the conduction channel. Focused ion beam (FIB, FEI Quanta 3D FEG) was utilized for the deposition of Pt contacts. The dark current-voltage (i$_d$-V) curves and photoconductive measurements of the photodetector were carried out in a four-point probe electrical measurement system using Keithly 4200-SCS. A 532 nm laser source was used for illumination and the incident laser power was measured using a calibrated power meter (Ophir Nova II) with a silicon photodiode head (Ohir PD300-UV). A holographic diffuser was utilized to minimize the error in the power density calculation by broadening the laser beam size (~20 mm^2).

3. Results and Discussion

3.1. WS$_2$ Crystal Characterization

The XRD pattern of CVT-grown WS$_2$ crystal is shown in Figure 1a. The observed diffraction peaks at 2θ values of 14.3, 28.9, 43.9, and 59.8° are assigned to the (002), (004),

(006), and (008) planes, respectively. The positions of sharp Bragg reflections confirm the 2H phase of WS_2 crystals according to JCPDS card no. 08-0237 [42,43]. The 2H WS_2 crystal lattice belongs to the $P6_3/mmc$ (D_{6h}^4) hexagonal space group that has space inversion symmetry [44]. The observed sharp and narrow peaks are an indication of the high crystal quality of WS_2 crystals grown by the CVT technique. All diffraction peaks along the (00l) direction denote that the crystal growth is along the *c*-axis and the major preferential orientation is along the (002) plane. The absence of any binary or impurity phases in the XRD pattern demonstrates the exceptional quality of the CVT-grown crystals.
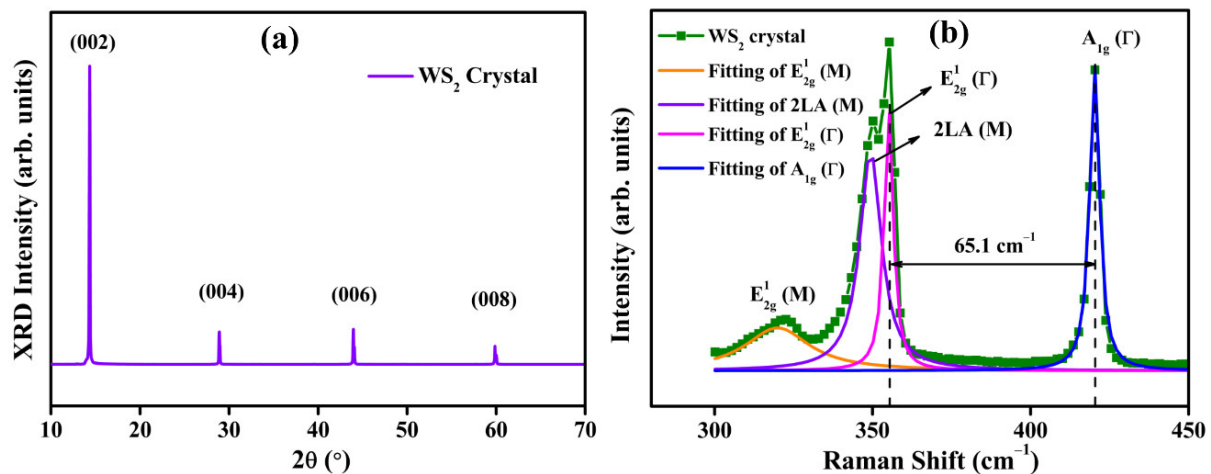
Figure 1. Structural characterization of CVT-grown WS_2 bulk crystal. (**a**) X-ray diffraction pattern and (**b**) Raman spectrum.

Figure 1b depicts the Raman spectrum of CVT-grown WS_2 layered crystal. The multi-peak Lorentzian fitting is used for the individual peaks fitting and also for the deconvolution of a broad peak obtained at around 350 cm^{-1}, which clearly separates the individual peaks from the overlapping. The observed Raman peaks at 319.9, 349.3, 355.1, and 420.2 cm^{-1} are attributed to E_{2g}^1 (M), 2LA (M), E_{2g}^1 (Γ), and A_{1g} (Γ) modes of WS_2 crystal, respectively [45–47]. The first-ordered dominant modes E_{2g}^1 (Γ) and A_{1g} (Γ) are most commonly observed for 2H WS_2 crystals [43,44,48]. The E_{2g}^1 mode is due to the in-plane vibrations of tungsten and sulfur atoms in the opposite direction, and the A_{1g} mode is due to the out-of-plane vibrations in sulfur atoms. The separation between these two modes is 65.1 cm^{-1}, which is consistent with the bulk WS_2, and the separation reduces gradually with the decrease of the number of layers [48,49]. The second-order longitudinal acoustic mode 2LA (M) is very close to the E_{2g}^1 (Γ) and sometimes it overlaps the E_{2g}^1 (Γ) mode [45]. The full-width half maxima of 2LA, E_{2g}^1, and A_{1g} modes are 8.3, 3.4, and 3.7 cm^{-1}, respectively, and it denotes the high crystallinity of WS_2 crystals grown by the CVT technique.

3.2. WS$_2$ Nanoflake Device Characterization

The thickness of the WS_2 nanoflakes was calculated using the AFM height profile measurement as shown in Figure 2a. The thickness of a typical nanoflake is 155 ± 5 nm. The inset of Figure 2a shows the AFM picture of the WS_2 nanoflake device with Pt contacts. The blue dotted line across the device denotes the position of the height profile measurement. Figure 2b depicts the i_d-V characteristics of a typical WS_2 nanoflake device in the range of −0.1 to +0.1 V. The linear i_d-V curve confirms the ohmic contact between the WS_2 nanoflake and FIB-deposited Pt contacts. The inset of Figure 2b represents the SEM image of the WS_2

nanoflake device that is used to calculate the dimensions of the device. The conductivity (σ) of the WS$_2$ nanoflake with a thickness of 230 nm was calculated using the relation [50,51]

$$\sigma = G\frac{l}{A} = G\frac{l}{wt} \tag{1}$$

where G is the electrical conductance and l, w, and t are the length, width, and thickness of the conduction channel. G is given by I/V, which is obtained from the slope of i$_d$-V curve, and the value is $1.69 \times 10^{-4}\ \Omega^{-1}$. The l and w are 4.22 μm and 2.65 μm, respectively, obtained from the SEM image of the nanoflake device with a thickness of 230 nm. The calculated conductivity of a typical nanoflake is $12\ \Omega^{-1}\text{cm}^{-1}$.
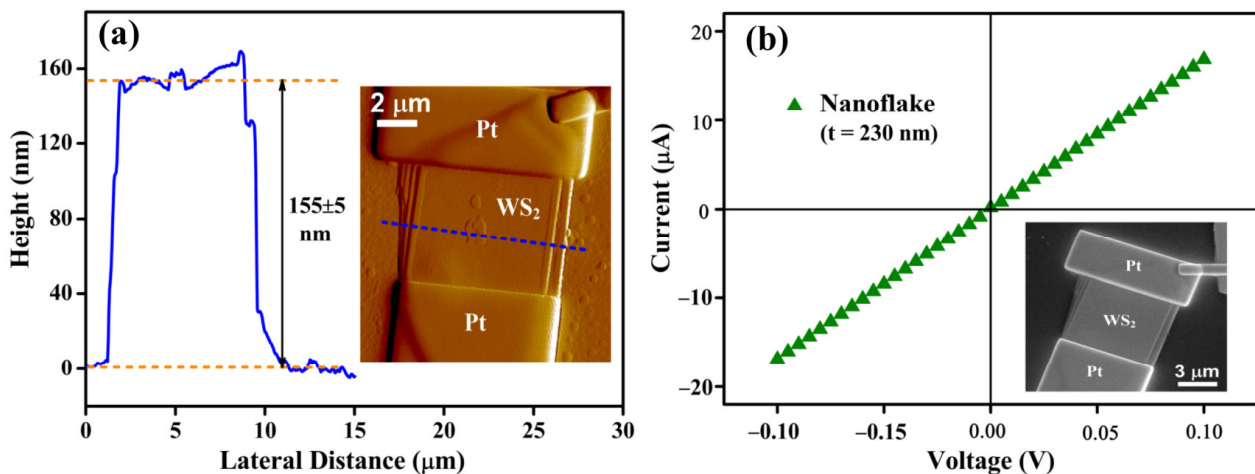

Figure 2. (**a**) AFM height profile of a WS$_2$ nanoflake with a thickness of 155 nm; inset shows the AFM image of the respective device. (**b**) i$_d$−V curve of a typical WS$_2$ nanoflake with a thickness of 230 nm; inset shows SEM image of the WS$_2$ nanoflake device of thickness 155 nm.

### 3.3. Photoconduction Properties of WS$_2$ Nanoflake

Figure 3 depicts the photoresponse of a WS$_2$ nanoflake with a thickness of 25 nm modulated by light power at an excitation wavelength of 532 nm. The photocurrent was measured for different light powers varying from 2 to 100 mW. A constant biasing voltage of 1 V was applied for the measurement of photocurrent as a function of time. First, we have recorded one cycle of photocurrent response for each light power separately. Next, the photocurrent measurements of different powers were combined to clearly present the change in photocurrent with respect to different powers. The ON and OFF states denote the laser light conditions for single light power. When the laser was turned on, the photocurrent increased quickly, and we waited until it saturated. Once it reached saturation, the laser was turned off, and the photocurrent was dropped immediately and then reached saturation. The background dark current was subtracted from photoresponse curves to represent the photocurrent curves. It is clear from the photoresponse curves that the photocurrent increases with the increase of light power. Generally, a large number of photons of high light intensity create a higher number of electron-hole pairs, and thus the photocurrent increases. The periodic nature of the photoresponse curve under different light powers is an indication of good stability and reproducibility of fabricated WS$_2$ devices. With the increase of light power up to 100 mW, we did not observe any photocurrent saturation in the WS$_2$ nanoflake, and hence the WS$_2$ photodetectors can be suitable for operation in the linear region.
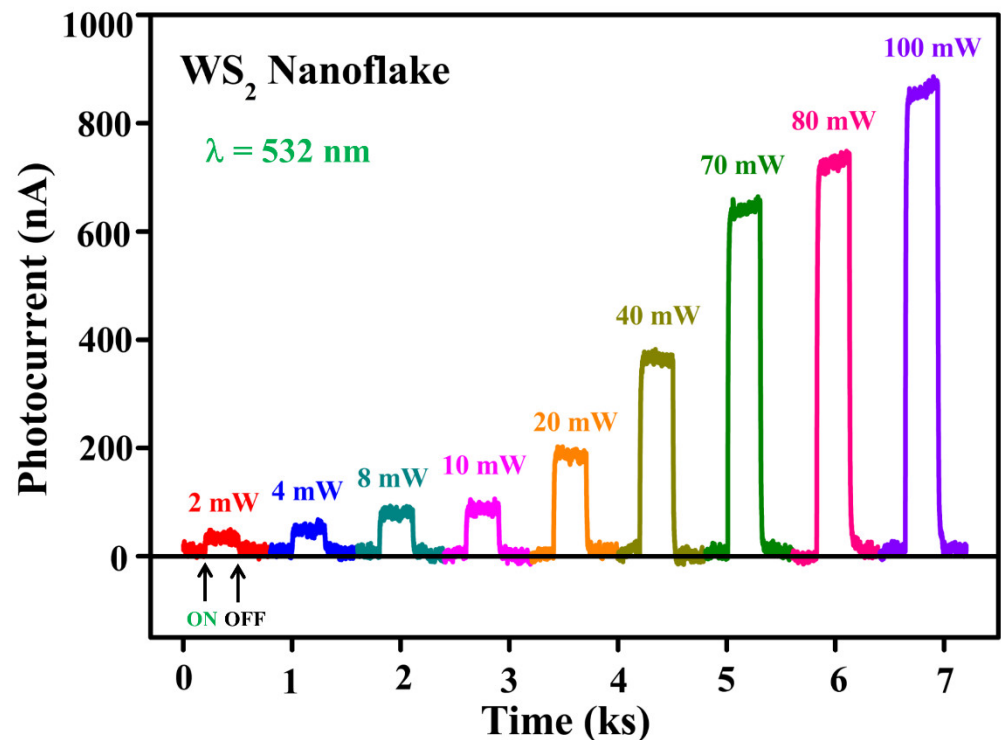
Figure 3. Photocurrent response of a WS$_2$ nanoflake under laser illumination of a wavelength of 532 nm. The photocurrent is measured as a function of time under various powers at a fixed bias voltage of 1 V. The ON/OFF denotes the laser light condition.

To interpret the significant dependence of the photocurrent on the illumination intensity, the plot drawn between the photocurrent and light intensity in the range of 80–4000 Wm^{-2} is shown in Figure 4a. The photocurrent strongly depends on the light intensity, and the experimental data can be fitted using a power law given by $i_p = aP^\beta$, where i_p is the photocurrent, a is the scaling constant, P is the light power, and β is an exponent [52]. The power law is well-fitted to the experimental data with $\beta = 0.99$. Generally, β values are in the range of 0 to 1. The deviation of the β value from unity is the indication of the presence of complex processes such as generation, trapping, and recombination of electron-hole within the semiconductor [53]. In our case, the β value is near unity, which indicates that the exfoliated WS$_2$ nanoflake was of high quality with very few defects [54].
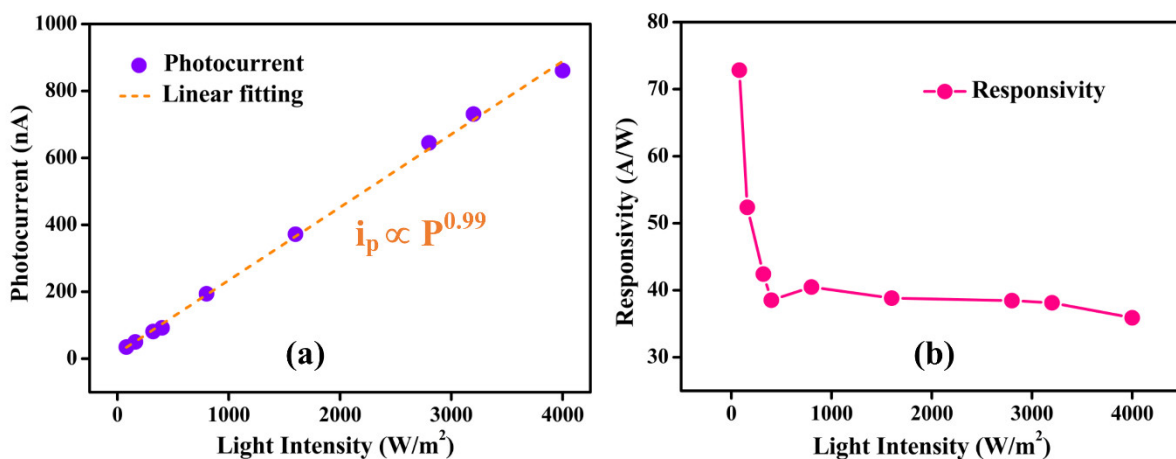
Figure 4. The dependence of (**a**) photocurrent and (**b**) responsivity on incident light intensities from 80 to 4000 Wm^{-2}. The photocurrent data points were fitted using linear function.

The photodetectors were characterized by several crucial parameters such as responsivity (R), gain (Γ), and normalized gain (Γ_n) to evaluate their performance. The R is one of the most important figure-of-merits, which is a measure of the photodetector's electrical response to the incident light and is obtained from the formula [7]

$$R = \frac{i_p}{P} \tag{2}$$

where, i_p is the photocurrent and P is the laser power incident on the projected area (A) of a photodetector, and it is given by $P = IA = Iwl$, where I is the light intensity and w and l are the width and length of the conducting channel, respectively [55]. The R values as a function of light intensity are shown in Figure 4b. We noted that R is sensitive to the lower light intensity (80–320 Wm^{-2}) and insensitive to the higher light intensities (400–4000 Wm^{-2}). R decreases with the increase of light intensity from 80 to 400 Wm^{-2}, and a further increase of light intensity up to 4000 Wm^{-2} results in an almost constant R value. A similar dependency of R on light intensity was observed in WS$_2$ monolayer [56] and SnS/rGO [57] photodetectors. The calculated R values are in the range of 36–73 AW^{-1}, and this high responsivity may be due to the efficient absorption and optimized WS$_2$ nanoflake device configuration. These values are higher than the other photodetectors based on 2D materials such as NbSe$_2$ nanoflakes (R~2.3–3.8 AW^{-1}) [50], MoS$_2$ nanoflakes (R~20–30 AW^{-1}) [58], and NbS$_2$ nanoflakes (R~0.6 AW^{-1}) [59]. The largest R value (73 AW^{-1}) at lower light intensity (80 Wm^{-2}) is owed to the weak recombination of photo-excited carriers [60].

Gain (Γ) is another figure-of-merit of photodetectors that determine the circulating number of photo carriers moving through a photoconductor per unit time before recombination. It is given by the ratio of the carrier lifetime (τ) to the transit time (τ_t) between the electrodes [50,61].

$$\Gamma = \frac{\tau}{\tau_t} = \frac{V}{l^2}\tau\mu \tag{3}$$

where, l is the electrodes inter distance, μ is the mobility, and V is the applied voltage. Γ linearly depends on R and it can be calculated using the formula [62,63]

$$\Gamma = \frac{R}{\eta}\frac{h\nu}{q} \tag{4}$$

where, η is the external quantum efficiency, q is the charge of an electron, h is Planck's constant, and ν is the frequency of the photon. The η value was calculated using the formula $\eta = 1 - e^{-\alpha t}$, where α is the absorption coefficient at the wavelength of 532 nm (2.33 eV) and t is the thickness of the nanoflake [50,58]. The reflection loss was eliminated to simply the η calculation. The α value of WS$_2$ bulk is ~2×10^5 cm^{-1} at a photon energy of 2.33 eV [64,65]. By considering the nanoflake thickness of 25 nm, the calculated η value is 0.39 (39%).

The determined Γ values as a function of light intensity are shown in Figure 5a. The Γ values follow a similar trend to R. The obtained Γ values are in the range of 215–436, with variation of light intensity from 80 to 4000 Wm^{-2}. The Γ decreases with the increase of light intensity up to 400 Wm^{-2}, and a further increase of light intensity up to 4000 Wm^{-2} leads to saturation in the Γ values. This may be attributed to the continuous filling of trap states upon illumination. Suppose the trap states are filled completely at a certain intensity of light, the excess electrons created by the higher light intensity cannot be trapped and thus decrease the average carrier lifetime. Hence, the photoconductive gain was reduced [4]. The Γ values (215–436) of our photodetector are superior to the reported photodetectors based on the MoS$_2$ nanoflake (Γ~66–103) [58], WS$_2$/Au NPs (Γ~30) [66], and the phototransistors based on MoS$_2$ (Γ~0.2) and MoSe$_2$ (Γ~5×10^{-4}) [67].
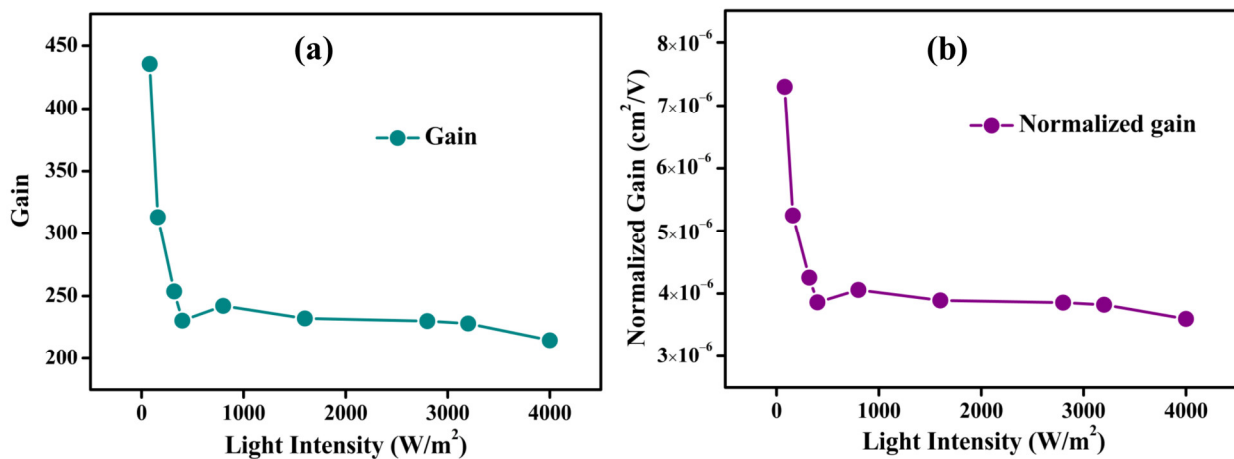
Figure 5. Variation of (**a**) gain and (**b**) normalized gain of a WS$_2$ nanoflake photodetector with a variation of light intensity from 80 to 4000 Wm^{-2}.

Normalized gain (Γ_n) is independent of device geometry and can be considered a fair figure-of-merit to compare the performance of other devices. The photoconduction process is mainly involving the light absorption and movement of carriers between the electrodes. Numerous factors including carrier mobility, lifetime, applied bias, distance between electrodes, and efficiency of light absorption may affect the performance of photodetectors. Γ_n is a measure of the intrinsic photoconductivity of the device and is given by the product of η, τ, and μ [61,68].

$$\Gamma_n = \eta\tau\mu = \eta\frac{\Gamma}{(V/l^2)} = \frac{E}{q}\frac{l^2}{V}R \tag{5}$$

Figure 5b depicts the Γ_n values as a function of light intensity. The Γ_n values follow the Γ trend and the calculated values are in the range of 3.5–7.3 × 10^{-6} cm^{2}V^{-1}. The obtained values are higher than the AuNRs/MoS$_2$/graphene device (Γ_n~8.63 × 10^{-7} cm^{2}V^{-1}) [68] but lower than the MoS$_2$-UCNP nanocomposite (Γ_n~1.48 × 10^{-4} cm^{2}V^{-1}) [61] and InSe (Γ_n~3.2 cm^{2}V^{-1}) [55] based photodetectors. The moderate Γ_n values of our device required further investigation of other parameters such as carrier lifetime and mobility.

The photodetector parameters Γ and Γ_n were rarely investigated for the 2D material photodetectors. Hence, the comparison of devices based on Γ and Γ_n becomes tough. We have compared our device performance with other reported WS$_2$ photodetectors fabricated by different methods based on their operation region of wavelength, biasing voltage, and responsivity as summarized in Table 1. It is noticed that the WS$_2$ nanoflake device obtained in the present work shows better responsivity at a lower bias voltage of 1 V. The high responsivity of our device also outperformed some CVD-grown WS$_2$ monolayer-based photodetectors, and hence the WS$_2$ nanoflakes can be a potential candidate for fabricating novel optoelectronic devices.

Table 1. Comparison of WS$_2$ photodetectors based on responsivity, fabrication method, and their operational wavelength with bias voltage.

Material	Fabrication Method	Wavelength (nm)	Bias Voltage (V)	Responsivity (AW^{-1})	Reference
WS$_2$ nanoflake	Exfoliation	532	1	73	Present work
WS$_2$ nanosheets	Hydrothermal intercalation	532	5	4 × 10^{-3}	[19]
WS$_2$ films	PLD	635	9	0.51	[26]
WS$_2$ nanofilm	Sputtering	365	5	53.3	[52]
WS$_2$ monolayer	CVD	532	10	0.52 × 10^{-3}	[56]
WS$_2$ monolayer	CVD	500	1	7.3	[69]
WS$_2$ multilayer	CVD	458–647	5	92 × 10^{-6}	[70]

4. Conclusions

We successfully fabricated a visible photodetector using exfoliated WS$_2$ nanoflakes and explored its photoconduction properties. The photocurrent increases with the increase of light intensity from 80 to 4000 Wm^{-2} and is well-fitted to the power law with an exponent value of 0.99. The photoresponsivity decreases with the increase of light intensity from 80 to 400 Wm^{-2}, and a further increase of light intensity up to 4000 Wm^{-2} results in an almost constant R value. The fabricated device showed a stable photoresponse with some reproducible characteristics. The device exhibited good responsivity in the range of 36–73 AW^{-1}, and the normalized gain was in the range of 3.5–7.3 $\times$ 10^{-6} cm^{2}V^{-1} at a lower biasing voltage of 1 V. The obtained excellent photodetector parameters suggest a promising application of WS$_2$ nanoflakes in future novel optoelectronic devices.

References

1. Yang, W.; Hu, K.; Teng, F.; Weng, J.; Zhang, Y.; Fang, X. High-Performance Silicon-Compatible Large-Area UV-to-Visible Broadband Photodetector Based on Integrated Lattice-Matched Type II Se/n-Si Heterojunctions. *Nano Lett.* **2018**, *18*, 4697–4703. [CrossRef] [PubMed]
2. Basyooni, M.A.; Zaki, S.E.; Alfryyan, N.; Tihtih, M.; Eker, Y.R.; Attia, G.F.; Yılmaz, M.; Ateş, Ş.; Shaban, M. Nanostructured MoS$_2$ and WS$_2$ Photoresponses under Gas Stimuli. *Nanomaterials* **2022**, *12*, 3585. [CrossRef] [PubMed]
3. Dam, S.; Saha, A.; Hussain, S. Photoresponse Properties of Thin Films of Vertically Grown WS$_2$ Nanoflakes. *Mater. Sci. Eng. B Solid-State Mater. Adv. Technol.* **2022**, *277*, 115587. [CrossRef]
4. Fang, H.; Hu, W. Photogating in Low Dimensional Photodetectors. *Adv. Sci.* **2017**, *4*, 1700323. [CrossRef] [PubMed]
5. Xie, C.; Mak, C.; Tao, X.; Yan, F. Photodetectors Based on Two-Dimensional Layered Materials Beyond Graphene. *Adv. Funct. Mater.* **2017**, *27*, 1603886. [CrossRef]
6. Ghanghass, A.; Sameera, I.; Bhatia, R. Multi-Layer Growth of Tungsten Disulphide Using Thermal Chemical Vapour Deposition. *Mater. Today Proc.* **2023**, *74*, 197–201. [CrossRef]
7. Tan, H.; Fan, Y.; Zhou, Y.; Chen, Q.; Xu, W.; Warner, J.H. Ultrathin 2D Photodetectors Utilizing Chemical Vapor Deposition Grown WS$_2$ with Graphene Electrodes. *ACS Nano* **2016**, *10*, 7866–7873. [CrossRef]
8. Choi, W.; Choudhary, N.; Han, G.H.; Park, J.; Akinwande, D.; Lee, Y.H. Recent Development of Two-Dimensional Transition Metal Dichalcogenides and Their Applications. *Mater. Today* **2017**, *20*, 116–130. [CrossRef]
9. Wang, H.; Yu, L.; Lee, Y.H.; Shi, Y.; Hsu, A.; Chin, M.L.; Li, L.J.; Dubey, M.; Kong, J.; Palacios, T. Integrated Circuits Based on Bilayer MoS$_2$ Transistors. *Nano Lett.* **2012**, *12*, 4674–4680. [CrossRef]
10. Jariwala, D.; Sangwan, V.K.; Lauhon, L.J.; Marks, T.J.; Hersam, M.C. Emerging Device Applications for Semiconducting Two-Dimensional Transition Metal Dichalcogenides. *ACS Nano* **2014**, *8*, 1102–1120. [CrossRef]
11. Zhu, W.; Low, T.; Wang, H.; Ye, P.; Duan, X. Nanoscale Electronic Devices Based on Transition Metal Dichalcogenides. *2D Mater.* **2019**, *6*, 032004. [CrossRef]
12. Yin, Z.; Li, H.; Li, H.; Jiang, L.; Shi, Y.; Sun, Y.; Lu, G.; Zhang, Q.; Chen, X.; Zhang, H. Single-Layer MoS$_2$ Phototransistors. *ACS Nano* **2012**, *6*, 74–80. [CrossRef] [PubMed]
13. Choi, W.; Cho, M.Y.; Konar, A.; Lee, J.H.; Cha, G.B.; Hong, S.C.; Kim, S.; Kim, J.; Jena, D.; Joo, J.; et al. High-Detectivity Multilayer MoS$_2$ Phototransistors with Spectral Response from Ultraviolet to Infrared. *Adv. Mater.* **2012**, *24*, 5832–5836. [CrossRef] [PubMed]

14. Tsai, D.S.; Liu, K.K.; Lien, D.H.; Tsai, M.L.; Kang, C.F.; Lin, C.A.; Li, L.J.; He, J.H. Few-Layer MoS$_2$ with High Broadband Photogain and Fast Optical Switching for Use in Harsh Environments. *ACS Nano* **2013**, *7*, 3905–3911. [CrossRef]

15. Aji, A.S.; Solís-Fernández, P.; Ji, H.G.; Fukuda, K.; Ago, H. High Mobility WS$_2$ Transistors Realized by Multilayer Graphene Electrodes and Application to High Responsivity Flexible Photodetectors. *Adv. Funct. Mater.* **2017**, *27*, 1703448. [CrossRef]

16. Lan, C.; Li, C.; Yin, Y.; Liu, Y. Large-Area Synthesis of Monolayer WS$_2$ and Its Ambient-Sensitive Photo-Detecting Performance. *Nanoscale* **2015**, *7*, 5974–5980. [CrossRef] [PubMed]

17. Li, H.J.W.; Huang, K.; Zhang, Y. Enhanced Photoresponsivity of the GOQDs Decorated WS$_2$ Photodetector. *Mater. Res. Express* **2019**, *6*, 045902. [CrossRef]

18. Pawbake, A.S.; Waykar, R.G.; Late, D.J.; Jadkar, S.R. Highly Transparent Wafer-Scale Synthesis of Crystalline WS$_2$ Nanoparticle Thin Film for Photodetector and Humidity-Sensing Applications. *ACS Appl. Mater. Interfaces* **2016**, *8*, 3359–3365. [CrossRef] [PubMed]

19. Li, J.; Han, J.; Li, H.; Fan, X.; Huang, K. Large-Area, Flexible Broadband Photodetector Based on WS$_2$ Nanosheets Films. *Mater. Sci. Semicond. Process.* **2020**, *107*, 104804. [CrossRef]

20. Yang, Y.; Liu, G.; Li, P.; Zhang, M.; Wang, J.; Hu, W.; Xue, Z.; Di, Z. High-Performance Broadband Tungsten Disulfide Photodetector Decorated with Indium Arsenide Nanoislands. *Phys. Status Solidi Appl. Mater. Sci.* **2020**, *217*, 2000297. [CrossRef]

21. Ahmad, H.; Thandavan, T.M.K. Ultraviolet Photoconduction in Tungsten Disulphide Based Schottky Heterostructure Photodetector. *Opt. Mater.* **2019**, *92*, 255–261. [CrossRef]

22. Yadav, P.V.K.; Ashok Kumar Reddy, Y. Controlled Two-Step Synthesis of Nanostructured WS$_2$ Thin Films for Enhanced UV–Visible Photodetector Applications. *Sens. Actuators A Phys.* **2022**, *345*, 113780. [CrossRef]

23. Rivera, A.M.; Gaur, A.P.S.; Sahoo, S.; Katiyar, R.S. Studies on Chemical Charge Doping Related Optical Properties in Monolayer WS$_2$. *J. Appl. Phys.* **2016**, *120*, 105102. [CrossRef]

24. Perrozzi, F.; Emamjomeh, S.M.; Paolucci, V.; Taglieri, G.; Ottaviano, L.; Cantalini, C. Thermal Stability of WS$_2$ Flakes and Gas Sensing Properties of WS$_2$/WO$_3$ Composite to H$_2$, NH$_3$ and NO$_2$. *Sens. Actuators B Chem.* **2017**, *243*, 812–822. [CrossRef]

25. Liu, L.; Kumar, S.B.; Ouyang, Y.; Guo, J. Performance Limits of Monolayer Transition Metal Dichalcogenide Transistors. *IEEE Trans. Electron. Devices* **2011**, *58*, 3042–3047. [CrossRef]

26. Yao, J.D.; Zheng, Z.Q.; Shao, J.M.; Yang, G.W. Stable, Highly-Responsive and Broadband Photodetection Based on Large-Area Multilayered WS$_2$ Films Grown by Pulsed-Laser Deposition. *Nanoscale* **2015**, *7*, 14974–14981. [CrossRef] [PubMed]

27. Esfandiari, M.; Mohajerzadeh, S. Formation of Large Area WS$_2$ Nanosheets Using an Oxygen-Plasma Assisted Exfoliation Suitable for Optical Devices. *Nanotechnology* **2019**, *30*, 204. [CrossRef] [PubMed]

28. Park, J.; Lee, W.; Choi, T.; Hwang, S.H.; Myoung, J.M.; Jung, J.H.; Kim, S.H.; Kim, H. Layer-Modulated Synthesis of Uniform Tungsten Disulfide Nanosheet Using Gas-Phase Precursors. *Nanoscale* **2015**, *7*, 1308–1313. [CrossRef]

29. Georgiou, T.; Jalil, R.; Belle, B.D.; Britnell, L.; Gorbachev, R.V.; Morozov, S.V.; Kim, Y.J.; Gholinia, A.; Haigh, S.J.; Makarovsky, O.; et al. Vertical Field-Effect Transistor Based on Graphene-WS$_2$ Heterostructures for Flexible and Transparent Electronics. *Nat. Nanotechnol.* **2013**, *8*, 100–103. [CrossRef]

30. Huo, N.; Yang, S.; Wei, Z.; Li, S.S.; Xia, J.B.; Li, J. Photoresponsive and Gas Sensing Field-Effect Transistors Based on Multilayer WS$_2$ Nanoflakes. *Sci. Rep.* **2014**, *4*, 5209. [CrossRef]

31. Mohan, V.V.; Manuraj, M.; Anjana, P.M.; Rakhi, R.B. WS$_2$ Nanoflowers as Efficient Electrode Materials for Supercapacitors. *Energy Technol.* **2022**, *10*, 2100976. [CrossRef]

32. Sheng, Y.; Chen, T.; Lu, Y.; Chang, R.J.; Sinha, S.; Warner, J.H. High-Performance WS$_2$ Monolayer Light-Emitting Tunneling Devices Using 2D Materials Grown by Chemical Vapor Deposition. *ACS Nano* **2019**, *13*, 4530–4537. [CrossRef] [PubMed]

33. Hasani, A.; Nguyen, T.P.; Tekalgne, M.; VanLe, Q.; Choi, K.S.; Lee, T.H.; Jung Park, T.; Jang, H.W.; Kim, S.Y. The Role of Metal Dopants in WS$_2$ Nanoflowers in Enhancing the Hydrogen Evolution Reaction. *Appl. Catal. A Gen.* **2018**, *567*, 73–79. [CrossRef]

34. Li, Y.; Chernikov, A.; Zhang, X.; Rigosi, A.; Hill, H.M.; Van DerZande, A.M.; Chenet, D.A.; Shih, E.M.; Hone, J.; Heinz, T.F. Measurement of the Optical Dielectric Function of Monolayer Transition-Metal Dichalcogenides: MoS$_2$, MoSe$_2$, WS$_2$, and WSe$_2$. *Phys. Rev. B—Condens. Matter Mater. Phys.* **2014**, *90*, 205422. [CrossRef]

35. Palik, E.D. *Handbook of Optical Constants of Solids III*; Academic Press: San Diego, CA, USA, 1998.

36. Yang, R.; Feng, S.; Xiang, J.; Jia, Z.; Mu, C.; Wen, F.; Liu, Z. Ultrahigh-Gain and Fast Photodetectors Built on Atomically Thin Bilayer Tungsten Disulfide Grown by Chemical Vapor Deposition. *ACS Appl. Mater. Interfaces* **2017**, *9*, 42001–42010. [CrossRef] [PubMed]

37. Kim, H.C.; Kim, H.; Lee, J.U.; Lee, H.B.; Choi, D.H.; Lee, J.H.; Lee, W.H.; Jhang, S.H.; Park, B.H.; Cheong, H.; et al. Engineering Optical and Electronic Properties of WS$_2$ by Varying the Number of Layers. *ACS Nano* **2015**, *9*, 6854–6860. [CrossRef]

38. Zhao, W.; Ghorannevis, Z.; Chu, L.; Toh, M.; Kloc, C.; Tan, P.-H.; Eda, G. Evolution of Electronic Structure in Atomically Thin Sheets of WS$_2$ and WSe$_2$. *ACS Nano* **2013**, *7*, 791–797. [CrossRef]

39. Roy, A.; Kalita, P.; Mondal, B. Structural, Spectroscopic and Electrical Properties of Liquid Phase Exfoliated Few Layered Two-Dimensional Tungsten Disulfide (WS$_2$) Using Anionic Surfactant. *J. Mater. Sci. Mater. Electron.* **2023**, *34*, 224. [CrossRef]

40. Hwan Lee, S.; Lee, D.; Sik Hwang, W.; Hwang, E.; Jena, D.; Jong Yoo, W. High-Performance Photocurrent Generation from Two-Dimensional WS$_2$ Field-Effect Transistors. *Appl. Phys. Lett.* **2014**, *104*, 193113. [CrossRef]

41. Huo, N.; Kang, J.; Wei, Z.; Li, S.S.; Li, J.; Wei, S.H. Novel and Enhanced Optoelectronic Performances of Multilayer MoS$_2$-WS$_2$ Heterostructure Transistors. *Adv. Funct. Mater.* **2014**, *24*, 7025–7031. [CrossRef]

42. Habib, M.; Khalil, A.; Muhammad, Z.; Khan, R.; Wang, C.; Rehman, Z.u.; Masood, H.T.; Xu, W.; Liu, H.; Gan, W.; et al. WX$_2$ (X=S, Se) Single Crystals: A Highly Stable Material for Supercapacitor Applications. *Electrochim. Acta* **2017**, *258*, 71–79. [CrossRef]

43. Lin, D.Y.; Shih, Y.T.; Lin, P.C.; Tseng, B.C.; Hwang, S.B.; Kao, M.C. Photoelectric Properties of Pristine and Niobium-Doped Tungsten Disulfide Layered Crystals. *Opt. Mater.* **2023**, *135*, 113310. [CrossRef]

44. Lan, C.; Li, C.; Ho, J.C.; Liu, Y. 2D WS$_2$: From Vapor Phase Synthesis to Device Applications. *Adv. Electron. Mater.* **2021**, *7*, 2000688. [CrossRef]

45. Zobeiri, H.; Xu, S.; Yue, Y.; Zhang, Q.; Xie, Y.; Wang, X. Effect of Temperature on Raman Intensity of nm-thick WS$_2$: Combined Effects of Resonance Raman, Optical Properties, and Interface Optical Interference. *Nanoscale* **2020**, *12*, 6064–6078. [CrossRef]

46. Berkdemir, A.; Gutiérrez, H.R.; Botello-Méndez, A.R.; Perea-López, N.; Elías, A.L.; Chia, C.I.; Wang, B.; Crespi, V.H.; López-Urías, F.; Charlier, J.C.; et al. Identification of Individual and Few Layers of WS$_2$ Using Raman Spectroscopy. *Sci. Rep.* **2013**, *3*, 1755. [CrossRef]

47. Sourisseau, C.; Cruege, F.; Fouassier, M.; Alba, M. Second-Order Raman Effects, Inelastic Neutron Scattering and Lattice Dynamics in 2H-WS$_2$. *Chem. Phys.* **1991**, *150*, 281–293. [CrossRef]

48. Zeng, H.; Liu, G.B.; Dai, J.; Yan, Y.; Zhu, B.; He, R.; Xie, L.; Xu, S.; Chen, X.; Yao, W.; et al. Optical Signature of Symmetry Variations and Spin-Valley Coupling in Atomically Thin Tungsten Dichalcogenides. *Sci. Rep.* **2013**, *3*, 2–6. [CrossRef]

49. Mitioglu, A.A.; Plochocka, P.; Deligeorgis, G.; Anghel, S.; Kulyuk, L.; Maude, D.K. Second-Order Resonant Raman Scattering in Single-Layer Tungsten Disulfide WS$_2$. *Phys. Rev. B—Condens. Matter Mater. Phys.* **2014**, *89*, 245442. [CrossRef]

50. Huang, Y.H.; Chen, R.S.; Zhang, J.R.; Huang, Y.S. Electronic Transport in NbSe$_2$ Two-Dimensional Nanostructures: Semiconducting Characteristics and Photoconductivity. *Nanoscale* **2015**, *7*, 18964–18970. [CrossRef]

51. Bangolla, H.K.; Siao, M.D.; Huang, Y.H.; Chen, R.S.; Žukauskaitė, A.; Palisaitis, J.; Persson, P.O.Å.; Hultman, L.; Birch, J.; Hsiao, C.L. Composition-Dependent Photoconductivities in Indium Aluminium Nitride Nanorods Grown by Magnetron Sputter Epitaxy. *Nanoscale Adv.* **2022**, *4*, 4886–4894. [CrossRef]

52. Zeng, L.; Tao, L.; Tang, C.; Zhou, B.; Long, H.; Chai, Y.; Lau, S.P.; Tsang, Y.H. High-Responsivity UV-Vis Photodetector Based on Transferable WS$_2$ Film Deposited by Magnetron Sputtering. *Sci. Rep.* **2016**, *6*, 20343. [CrossRef]

53. Kind, H.; Yan, H.; Messer, B.; Law, M.; Yang, P. Nanowire Ultraviolet Photodetectors and Optical Switches. *Adv. Mater.* **2002**, *14*, 158–160. [CrossRef]

54. Hafeez, M.; Gan, L.; Li, H.; Ma, Y.; Zhai, T. Large-Area Bilayer ReS$_2$ Film/Multilayer ReS$_2$ Flakes Synthesized by Chemical Vapor Deposition for High Performance Photodetectors. *Adv. Funct. Mater.* **2016**, *26*, 4551–4560. [CrossRef]

55. Yang, H.W.; Hsieh, H.F.; Chen, R.S.; Ho, C.H.; Lee, K.Y.; Chao, L.C. Ultraefficient Ultraviolet and Visible Light Sensing and Ohmic Contacts in High-Mobility InSe Nanoflake Photodetectors Fabricated by the Focused Ion Beam Technique. *ACS Appl. Mater. Interfaces* **2018**, *10*, 5740–5749. [CrossRef]

56. Lan, C.; Zhou, Z.; Zhou, Z.; Li, C.; Shu, L.; Shen, L.; Li, D.; Dong, R.; Yip, S.P.; Ho, J.C. Wafer-Scale Synthesis of Monolayer WS$_2$ for High-Performance Flexible Photodetectors by Enhanced Chemical Vapor Deposition. *Nano Res.* **2018**, *11*, 3371–3384. [CrossRef]

57. Zhuo, R.; Zuo, S.; Quan, W.; Yan, D.; Geng, B.; Wang, J.; Men, X. Large-Size and High Performance Visible-Light Photodetectors Based on Two-Dimensional Hybrid Materials SnS/RGO. *RSC Adv.* **2018**, *8*, 761–766. [CrossRef]

58. Shen, W.C.; Chen, R.S.; Huang, Y.S. Photoconductivities in MoS$_2$ Nanoflake Photoconductors. *Nanoscale Res. Lett.* **2016**, *11*, 124. [CrossRef]

59. Huang, Y.H.; Peng, C.C.; Chen, R.S.; Huang, Y.S.; Ho, C.H. Transport Properties in Semiconducting NbS$_2$ nanoflakes. *Appl. Phys. Lett.* **2014**, *105*, 093106. [CrossRef]

60. Hao, L.; Wang, Z.; Xu, H.; Yan, K.; Dong, S.; Liu, H.; Du, Y.; Wu, Y.; Liu, Y.; Dong, M. 2D SnSe/Si Heterojunction for Self-Driven Broadband Photodetectors. *2D Mater.* **2019**, *6*, 034004. [CrossRef]

61. Ghosh, S.; Chiang, W.C.; Fakhri, M.Y.; Wu, C.T.; Chen, R.S.; Chattopadhyay, S. Ultrasensitive Broadband Photodetector Using Electrostatically Conjugated MoS$_2$-Upconversion Nanoparticle Nanocomposite. *Nano Energy* **2020**, *67*, 104258. [CrossRef]

62. Fan, Y.; Zhou, Y.; Wang, X.; Tan, H.; Rong, Y.; Warner, J.H. Photoinduced Schottky Barrier Lowering in 2D Monolayer WS$_2$ Photodetectors. *Adv. Opt. Mater.* **2016**, *4*, 1573–1581. [CrossRef]

63. Zhang, W.; Huang, J.K.; Chen, C.H.; Chang, Y.H.; Cheng, Y.J.; Li, L.J. High-Gain Phototransistors Based on a CVD MoS$_2$ Monolayer. *Adv. Mater.* **2013**, *25*, 3456–3461. [CrossRef]

64. Ballif, C.; Regula, M.; Lévy, F. Optical and Electrical Properties of Semiconducting WS$_2$ Thin Films: From Macroscopic to Local Probe Measurements. *Sol. Energy Mater. Sol. Cells* **1999**, *57*, 189–207. [CrossRef]

65. Roy, S.; Bermel, P. Electronic and Optical Properties of Ultra-Thin 2D Tungsten Disulfide for Photovoltaic Applications. *Sol. Energy Mater. Sol. Cells* **2018**, *174*, 370–379. [CrossRef]

66. Liu, Y.; Huang, W.; Chen, W.; Wang, X.; Guo, J.; Tian, H.; Zhang, H.; Wang, Y.; Yu, B.; Ren, T.L.; et al. Plasmon Resonance Enhanced WS$_2$ Photodetector with Ultra-High Sensitivity and Stability. *Appl. Surf. Sci.* **2019**, *481*, 1127–1132. [CrossRef]

67. Chang, Y.H.; Zhang, W.; Zhu, Y.; Han, Y.; Pu, J.; Chang, J.K.; Hsu, W.T.; Huang, J.K.; Hsu, C.L.; Chiu, M.H.; et al. Monolayer MoSe$_2$ Grown by Chemical Vapor Deposition for Fast Photodetection. *ACS Nano* **2014**, *8*, 8582–8590. [CrossRef]

68. Tomar, D.S.; Ghosh, S.; Jhan, L.C.; Chattopadhyay, S. Gold Nanorod-Activated Graphene/MoS$_2$ Nanosheet-Based Photodetectors for Bidirectional Photoconductance. *ACS Appl. Nano Mater.* **2023**, *6*, 1783–1795. [CrossRef]

69. Chen, Y. Growth of a Large, Single-Crystalline WS$_2$ Monolayer for High-Performance Photodetectors by Chemical Vapor Deposition. *Micromachines* **2021**, *12*, 137. [CrossRef] [PubMed]
70. Perea-López, N.; Elías, A.L.; Berkdemir, A.; Castro-Beltran, A.; Gutiérrez, A.H.R.; Feng, S.; Lv, R.; Hayashi, T.; López-Urías, F.; Ghosh, S.; et al. Photosensor Device Based on Few-Layered WS$_2$ Films. *Adv. Funct. Mater.* **2013**, *23*, 5511–5517. [CrossRef]